

Identifying Land Subsidence Using Global Digital Elevation Models

Kazimierz Becek¹, Khairunnisa Haji Ibrahim², Çağlar Bayık³, Saygin abdikan³, Hakan Senol Kutoğlu⁴, Dariusz Glabicki¹, and Jan Blachowski¹

¹Wroclaw University of Science and Technology

²Universiti Brunei Darussalam

³Zonguldak Bulent Ecevit Universitesi

⁴Zonguldak Bulent Ecevit University

November 21, 2022

Abstract

Recent developments in space-based surveying methods of Earth's topography, including the differential synthetic aperture radar interferometry (DInSAR), increased the availability of options for monitoring of land subsidence. However, DInSAR methods require expert knowledge, specialized software, and are time-consuming. Here, we demonstrate that a land subsidence signal in the difference of freely available global digital elevation models (DEMs), e.g., SRTM and TanDEM-X, is identifiable using a simple statistical method. This finding opens up a venue to develop a dedicated computer application to identify land subsidence or uplift of the order > 20 mm yr. Such an application would allow for the monitoring of the impacts of underground mining, earthquakes, landslides, volcanic activities, and similar effects on the Earth's topography. This software will provide a useful and cost-effective approach to scan the global DEMs for the benefit of many land planning and management agencies around the world.

Identifying Land Subsidence Using Global Digital Elevation Models

K. Becek^{1*}, K. Ibrahim³, Ç. Bayık², S. Abdikan², H. S. Kutoğlu², D. Glabicki¹, and J. Blachowski¹

¹Wroclaw University of Science and Technology, Faculty of Geoengineering, Mining and Geology, Wroclaw, Poland.

²Zonguldak Bulent Ecevit University, Department of Geomatics Engineering, Zonguldak, Turkey.

³University of Brunei Darussalam, Faculty of Social Sciences, Brunei Darussalam.

*Corresponding author: Kazimierz Becek (kazimierz.becek@pwr.edu.pl)

ORCID: 0000-0003-1532-9725

Key Points:

- Land subsidence or uplift signals can be identified using digital elevation models.
- The difference between past and recent global digital elevation models reveals a land subsidence signal at the level of 20 mm yr⁻¹.
- Geoprocessing or an artificial intelligence approach can assist in identifying land deformations using dedicated software.

21 **Abstract**

22 Recent developments in space-based surveying methods of Earth's topography, including the
23 differential synthetic aperture radar interferometry (DInSAR), increased the availability of
24 options for monitoring of land subsidence. However, DInSAR methods require expert
25 knowledge, specialized software, and are time-consuming. Here, we demonstrate that a land
26 subsidence signal in the difference of freely available global digital elevation models (DEMs),
27 e.g., SRTM and TanDEM-X, is identifiable using a simple statistical method. This finding opens
28 up a venue to develop a dedicated computer application to identify land subsidence or uplift of
29 the order $> 20 \text{ mm yr}^{-1}$. Such an application would allow for the monitoring of the impacts of
30 underground mining, earthquakes, landslides, volcanic activities, and similar effects on the
31 Earth's topography. This software will provide a useful and cost-effective approach to scan the
32 global DEMs for the benefit of many land planning and management agencies around the world.

33

34 **Plain Language Summary**

35 Land deformation is common throughout the globe and can potentially cause immense damage
36 and loss. To monitor and manage incidences of land deformation, experts have developed a
37 range of approaches that use spatial data about the Earth's surface captured by space-based
38 satellites. However, most, if not all, of these approaches are costly and not readily available as
39 they require expert knowledge, specialized software, and enormous amounts of time and other
40 resources. Yet, we have found an alternative approach that uses freely available data in the form
41 of global digital elevation models. By applying a simple statistical method that calculates
42 differences in elevation of the same area between two considerably separate time periods, this
43 approach can isolate and identify areas of rupture, movement or other forms of deformation of
44 the Earth's topography as a result of natural events such as earthquakes and volcanic activities or
45 human-made activities such as underground mining. By developing a suitable software
46 application that uses this approach, the cost of detecting and monitoring land deformation can be
47 significantly reduced, thus improving land survey and management efforts around the world.

48 **1 Introduction**

49 Underground mining has been attributed to several undesirable physical effects on the
50 Earth's surface, including mining-induced land deformations and landslides. In populated areas,
51 underground mining can interfere with the anthropogenic infrastructure, leading to extensive
52 damage or destruction, and could endanger human safety. Some measures have been proposed to
53 mitigate the impacts of mining. Still, the successful implementation of these measures depends
54 on several factors, including financial constraints and local politics, as well as precise and
55 updated information on the spatial extent and velocity of land deformation. The latter can be
56 obtained thanks to recent developments in the spaceborne surveying methods of the Earth's
57 surface, including the Synthetic Aperture Radar Interferometry (InSAR) (Crosetto & Pasquali,
58 2008; Rosen et al., 2000), Differential Synthetic Aperture Radar Interferometry (DInSAR)
59 (Crosetto et al., 2000), Persistent Scatterers Synthetic Aperture Interferometry (PsInSAR)
60 (Ferretti et al., 2000; Ferretti et al., 2001) and the Small Baseline Subset (SBAS) InSAR method
61 (Berardino et al., 2002), which have significantly enriched the arsenal of surveying methods for
62 monitoring and investigating land deformation. However, SAR interferometry-based methods
63 require extensive computing resources and are time-consuming. In addition, these approaches

64 demonstrate some technical incompetence under certain circumstances when it comes to
65 detecting surface deformations. For instance, they cannot detect the North-South deformation
66 component, and create layover and shadowing problems that might also obstruct the results
67 depending on the topography. Alternatives are therefore needed that are not only simpler in
68 approach, more efficient and accurate, but also cost-effective in terms of the time required to
69 process the data.

70 In this contribution, we demonstrate that freely available global digital elevation models
71 (DEMs) can be used to identify land subsidence/uplift caused by mining activities. Our approach
72 is based on comparing digital elevation models that were captured at two distant moments,
73 during which time the deformation occurred. While this method is straightforward, it has perhaps
74 deterred others from developing it further because of the limitations of the vertical accuracy of
75 global DEMs on the order of a few meters and the magnitude of land deformations at the level of
76 submeters, sometimes larger. Nevertheless, we have managed to develop this approach by
77 performing the following tasks towards reaching the aim of this project:

- 78 • We developed a raster of mining-induced land deformation of a test area in Turkey using
79 the SBAS (Berardino et al., 2002) method.
- 80 • Using regression analysis and hypothesis testing, we calculated the difference between
81 the recent (2014) TanDEM-X DEM and the Shuttle Radar Topography Mission (SRTM)
82 elevation data product as the reference dataset for the deformation and no-deformation
83 regions.

84 Our calculations detected an identifiable signal in the differences between the DEMs,
85 which strongly correlated with the land deformations. This finding provides a strong impetus for
86 developing an application that can quickly and efficiently scan and calculate differences in
87 existing global DEMs and identify land deformations of both anthropogenic and natural origins
88 that have occurred during the first decade of the third millennia around the world.

89 **2 Materials and Methods**

90 **2.1 Area of Interests (AOI)**

91 The AOI is situated in the central northern part of Turkey. It borders the northern
92 coastline of the Black Sea and covers an area of 17.7 km to the east and 11.5 km to the west. The
93 geographic coordinates of the SW/NE corners of the AOI are (WGS84): (Lat/Lon): 41°24'44"/
94 31°43'24" and 41°31'04"/31°56'05". The topography is well developed. The average terrain
95 elevation is approximately 233 m a.m.s.l. The lowest and highest points are at sea level and 600
96 m a.m.s.l., respectively. The dominant land cover (approximately 75 %) is forest, of which 90 %
97 is comprised of the deciduous tree species. The coastal strip comprises of human settlements,
98 including transportation and industrial infrastructure; the largest settlements are Zonguldak and
99 Kozlu, with a total population of approximately 150,000 residents combined and are located in
100 the western section of AOI. The largest industrial facility is a large power plant at Çatalağzı and
101 located in the central north of the AOI. The main industry is underground mining of hard coal
102 located underneath the Zonguldak and Kozlu towns and also in the central part of AOI. Mining
103 has been conducted in the area for over 100 years (Arca et al., 2018). The mining operations
104 have been carried out at a depth of 400 m to 600 m. Over the years, many land deformation and

105 landslide events have been observed, leading to serious damage to properties and even to deaths
106 (Arca et al., 2018).

107 2.2 Data

108 2.2.1 Shuttle Radar Topography Mission (SRTM) Digital Elevation Data Product

109 The SRTM-1" (v.3) (SRTM) elevation data product is a well-known global DEM that has
110 been used for many types of geospatial studies in several branches of science. The space shuttle
111 "Endeavor" in February 2000 hosted the unique single-pass Synthetic Aperture Radar (SAR)
112 instrument to acquire the data for processing using the SAR interferometry (InSAR) method to
113 generate semi-global DEM. The SRTM data product is available at one- and three-arcsec
114 resolution (approximately 30 m or 90 m at the Equator). The three-arc second version was
115 produced by the averaging process of the original one arc-second model. The vertical accuracy
116 of SRTM DEM is approximately 2 m (one sigma - for horizontal surfaces), which is well over
117 the mission's requirement (Rabus et al., 2003; Becek 2008, 2014). Version 3 of the SRTM-1" is
118 used as a reference data set in this contribution. The horizontal reference system used is WGS84,
119 and the elevation is provided with reference to the Earth Gravity Model (EGM96). As the data
120 for the SRTM product was captured during the winter season in the northern hemisphere, the
121 deciduous forests were in the leaves-off state, allowing for partial penetration of vegetation by
122 the C-band microwaves of the SRTM mission SAR system (Becek, 2011).

123 2.2.2 TanDEM-X Digital Elevation Data Product

124 TanDEM-X 30m DEM (TDX) is an elevation data product developed from the data
125 captured by the TerraSAR-X/TanDEM-X mission (Krieger et al., 2007). Similar to the SRTM,
126 the TDX is a quasi-DSM representing the elevation of the terrain, including objects above the
127 ground and elevation of the phase center between the canopy and the terrain in vegetated areas
128 (Becek, 2011). The spatial resolution of the TDX models is one arcsec or approximately 30 m at
129 the Equator. This model was developed by one of the authors of the paper using bilinear
130 resampling of 0.4 arcsec resolution data provided by DLR as a part of a research project.
131 However, the TanDEM-X DEM can be downloaded at the 3" arcsec resolution from
132 <https://geoservice.dlr.de/web/dataguide/tdm90/> free of charge. The 0.4 arcsec DEM is available
133 as a commercial product known as WorldDEMTM (Becek et al., 2016). The vertical accuracy of
134 the TDX is approximately 2 m (one sigma), while the accuracy of the WorldDEMTM is
135 approximately 0.8 m (one sigma) (Becek et al., 2016). Since the source of the data for the TDX
136 and WorldDEMTM are the same, one can expect that the conclusions from this study are valid for
137 both models. The horizontal reference system for TDX is WGS84. The vertical datum is the
138 WGS84 ellipsoid. According to the metadata file of the TDX, the SAR data were acquired
139 during 27 passes of the satellites between 17/02/2011 and 27/08/2014 and then averaged. Fifteen
140 images were taken during the leaves-off state of vegetation (autumn to early spring). This further
141 means that a vegetation bias can be present in the TDX and be similar to that of SRTM.

142 2.2.3 Synthetic Aperture Radar (SAR) Data

143 To identify the deformations in AOI, we used the SAR data captured by the Copernicus
144 Sentinel 1A/B satellite mission (ESA, 2020). A total of 103 images acquired in the
145 Interferometric Wide-Swath (IW) mode from the descending orbit no. 65 were used in the study.
146 The images were acquired between Jan. 2018 and Oct. 2019.

147 2.2.4 Reference DEM

148 A high quality and recent DEM model (HQM) was used to calibrate the SRTM and TDX
 149 models. The HQM is a digital surface model (DSM) produced from stereo pairs of 2017 aerial
 150 photography. The original DSM was produced at the resolution of 0.45 m, but it was available to
 151 the authors at the resolution of 5 m. The vertical accuracy is 1.52 m (one sigma) (Yilmaz &
 152 Erdoğan, 2018). The HQM is referenced to the national heighting system of Turkey (orthometric
 153 system). The HQM was further downsampled using the bilinear method to one arcsec resolution
 154 as the investigated DEMs. The assessment of the vertical accuracy of the model was confirmed
 155 using the runway method [4], carried out at a few selected flat sites, including sports fields and a
 156 highway.

157 2.3 Methods

158 2.3.1 Small Baseline Subset (SBAS) method

159 The SBAS method is a version of the Differential SAR interferometry (DInSAR) method,
 160 (e.g., Lanari et al., 2007). The SBAS method was developed to monitor land deformation as a
 161 function of time (Berardino et al., 2002). This method allows for the estimation of the velocity of
 162 the deformation with an accuracy of approximately 5 mm yr⁻¹ (Casu et al., 2005, 2006; Lanari et
 163 al., 2007). The SBAS data processing procedure has been described by others (e.g., Ferretti et al.,
 164 2001; Hanssen, 2001; Rosen et al., 2000) and its applications include assessing land subsidence
 165 under big cities (Amelung et al., 1999; Lanari et al., 2004), monitoring land subsidence caused
 166 by groundwater level change (Normand & Heggy, 2015), monitoring volcano eruption (Lee et
 167 al., 2006), and assessing mining-induced land deformation (Goel & Adam, 2014). One of the
 168 initial SBAS processing steps is to form the interferograms based on pairs of images taken from
 169 different points on the orbit separated by the spatial baseline. The second condition for selecting
 170 the images for interferogram is to restrict the temporal baseline (time between two image
 171 acquisitions). A temporal baseline of shorter than 36 days and a spatial baseline shorter than 100
 172 m were adopted in our case. Given the conditions, a total of 326 interferograms were formed.
 173 The SRTM-1" DEM was used to subtract the topographic phase from interferograms - a step in
 174 the SBAS data processing. As a final result, the raster of the Line-of-Sight (LOS) deformation
 175 had been obtained. The LOS deformation is a composite vector of land subsidence and
 176 horizontal displacement. Since we processed the images from the descending orbit only, it is not
 177 possible to split the LOS vector into the north/east components. The resulting raster has a spatial
 178 resolution of approximately four arcsec. The interferometric calculation, as well as the SBAS
 179 processing, were performed in the GMTSAR software (Sandwell et al., 2011). The SNAPHU
 180 software was used to unwrap the interferograms (Chen & Zebker, 2001).

181 2.3.2 Vertical Accuracy Model of the DEMs Difference

182 The vertical accuracy statement of the DEMs provided in Sections 2.2.1 to 2.2.4 covers
 183 the instrument- and the environment-induced component of the elevation error only (Becek
 184 2008, 2014). These components do not include the contribution of the so-called target induced
 185 component, which depends on the size of the pixel and slope of the terrain. The contribution of
 186 these two variables can be calculated from Equation (1) (Becek 2008):

$$187 \quad \sigma^2 = \frac{1}{12} d^2 \tan^2(s), \quad (1)$$

188 where σ^2 is the variance of the target-induced error,
 189 d is pixel size, and
 190 s is the slope at a given pixel.

191 The target-induced error of a DEM for a given AOI is the arithmetic average of the errors
 192 of all pixels within the AOI.

193 To calculate the total vertical error of a DEM within a given AOI, we assume that the
 194 components of the error, e.g., the instrument-, environment-, and target-induced errors are
 195 statistically independent. Hence, the total vertical error can be estimated using Equation (2)
 196 [ibid]:

$$197 \quad \sigma_{total}^2 = \sigma_I^2 + \sigma_E^2 + \sigma_T^2, \quad (2)$$

198 where $\sigma_I^2, \sigma_E^2, \sigma_T^2$ are the variance of the instrument-, environment- and target-induced
 199 error.

200 In further considerations, we omitted the environment-induced error. In this study, we
 201 used the difference between the DEMs. To estimate the vertical error of the difference of two
 202 uncorrelated random variables (DEM₁ and DEM₂), we used the error propagation law expressed
 203 in a simple form as per Equation (3):

$$204 \quad \sigma_{diff}^2 = \sigma_{DEM1}^2 + \sigma_{DEM2}^2, \quad (3)$$

205 where $\sigma_{diff}^2, \sigma_{DEM1}^2, \sigma_{DEM2}^2$ is the variance of the error of difference, DEM₁, and DEM₂,
 206 respectively.

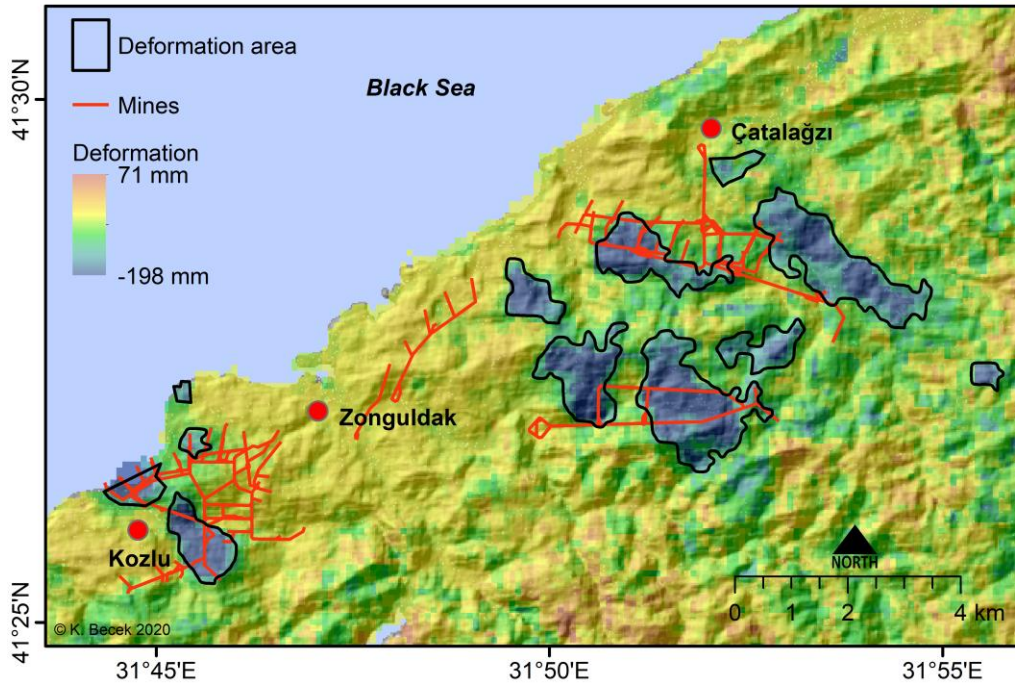
207 Note that we used here the term ‘variance’ as the second power of the ‘standard
 208 deviation.’ However, in a more general case, when there is a bias or systematic error in the
 209 difference between random variables ($\text{avg}(\text{DEM}_1 - \text{DEM}_2) \neq 0$), the correct term is the ‘mean
 210 squared error’ or MSE.

211 **3 Results**

212 3.1. Line-of-Sight (LOS) Deformation

213 Figure 1 shows a map of the LOS deformations in the AOI calculated for the period
 214 between January 2018 and October 2019. The locations of some of the mines (red solid line) are
 215 also shown on the map. The deformations appear to be closely associated with underground
 216 mining operations. In the northeastern and southern sections of the map, some uplift areas are
 217 visible. Avsar et al. (2017) suggest a tectonic uplift of up to 6 mm yr⁻¹ around the Black Sea
 218 region as a possible reason. In addition, the artifacts related to the low coherence may be due to
 219 vegetation.

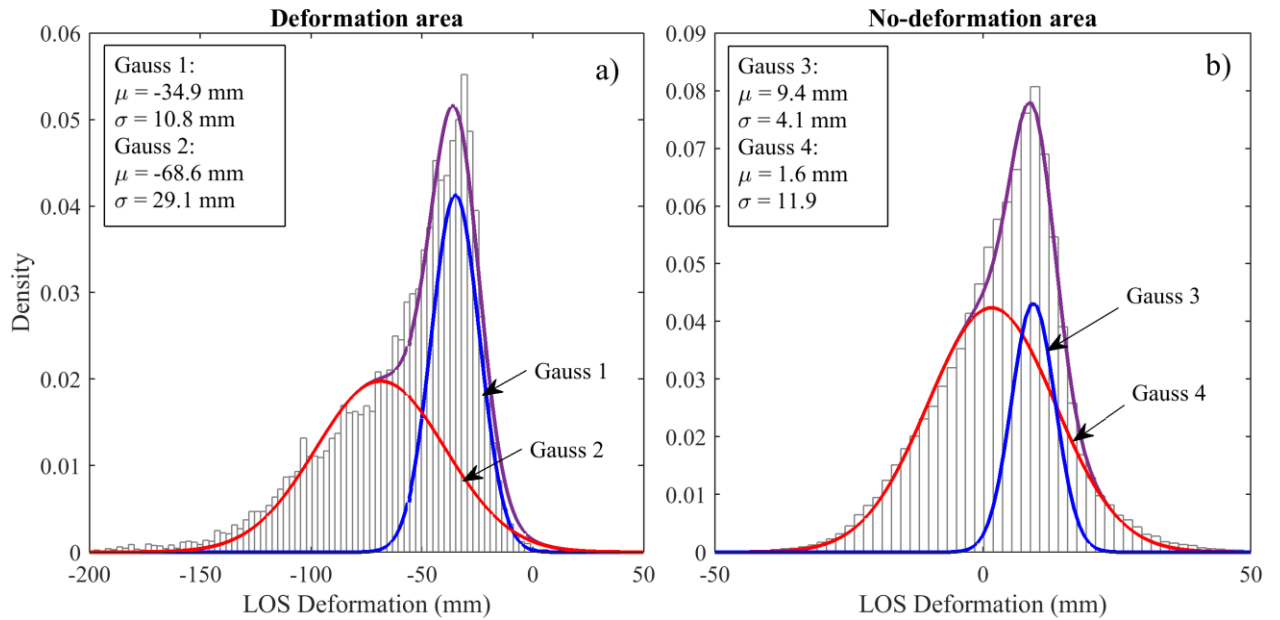
220



221

222 Figure 1 The Line of Sight (LOS) raster of deformation as a result of SBAS processing of the
 223 Copernicus Sentinel 1A/B SAR data. The deformations occurred between January 2018 and
 224 October 2019. The approximate location of the mining infrastructure is also shown.

225 The deformation areas were manually, and arbitrary outlined (solid black line). Figure 2 shows
 226 histograms of deformations for the deformation (a), and no-deformation areas (b), respectively.
 227 The histograms are bimodal (negative skew), suggesting that two random processes are
 228 contributing to the deformations. The histograms were modeled using the generalized Gaussian
 229 pdf. The analysis of the histograms helps to identify the origin of the underlying processes
 230 contributing to the deformation. Hence, the Gauss 1 and Gauss 3 curves in Figure 2 represent
 231 the measurement noise of the SBAS technique. Since the Gauss 1 curve also contains some
 232 residuals of the deformation signal, its standard deviation (10.8 mm) is higher than that of the
 233 Gauss 3 curve. This conclusion is consistent with the results found in, e.g., (Casu et al., 2005,
 234 2006; Lanari et al., 2007).



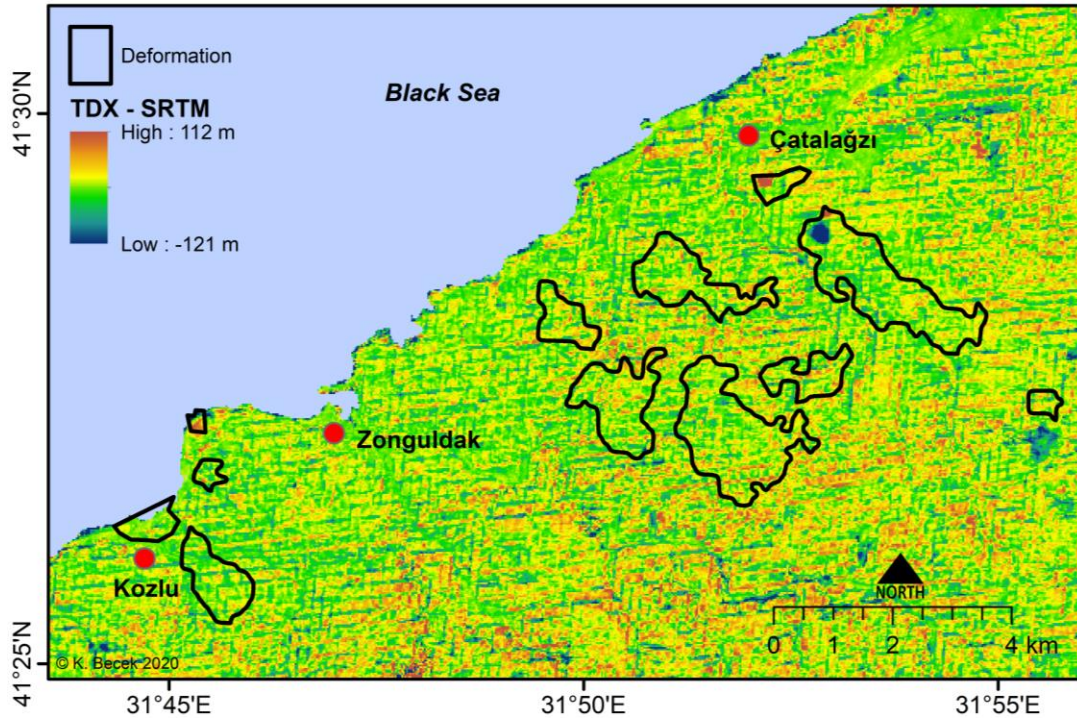
235

236 Figure 2 Histograms of the LOS deformation in a) the deformation area, and b) the no-
 237 deformation area Histograms are modeled using a two-term generalized Gaussian pdf. The mean
 238 and standard deviation are also shown. The negative skewness of the histogram indicates the
 239 presence of land subsidence in the AOI.

240 The curve Gauss 2 in Figure 2a represent the deformation in the deformation area. It
 241 reveals that the average deformation is -68.6 mm with the standard deviation of 29.1 mm, which
 242 translates to -3.4 mm yr^{-1} .

243 3.2. DEMs difference

244 The TDX and SRTM models exhibit elevation bias with respect to the local orthometric
 245 vertical reference systems. The source of this bias may be related to the calibration of SAR
 246 instruments, the precision of the EGM96 geoid model, and the characteristics of the local
 247 heighting system. Depending on the region of the world, the bias may be negative or positive and
 248 is of the order of one meter (Becek, 2014). To remove the bias from TDX and SRTM, we used a
 249 reference HQM. We corrected the DEMs by subtracting the average difference between both
 250 models and HQM with the opposite sign. We found that the bias for the TDX (including the
 251 geoid undulation) was 32.38 m (TDX was too high); the SRTM bias was -1.524 m (SRTM was
 252 too low). Figure 3 shows a map of differences between the (corrected) TDX and SRTM.



253

254

255

Figure 3. Map of the difference TDX *minus* SRTM. The SBAS-estimated location of deformation areas is also shown.

256

257

258

259

260

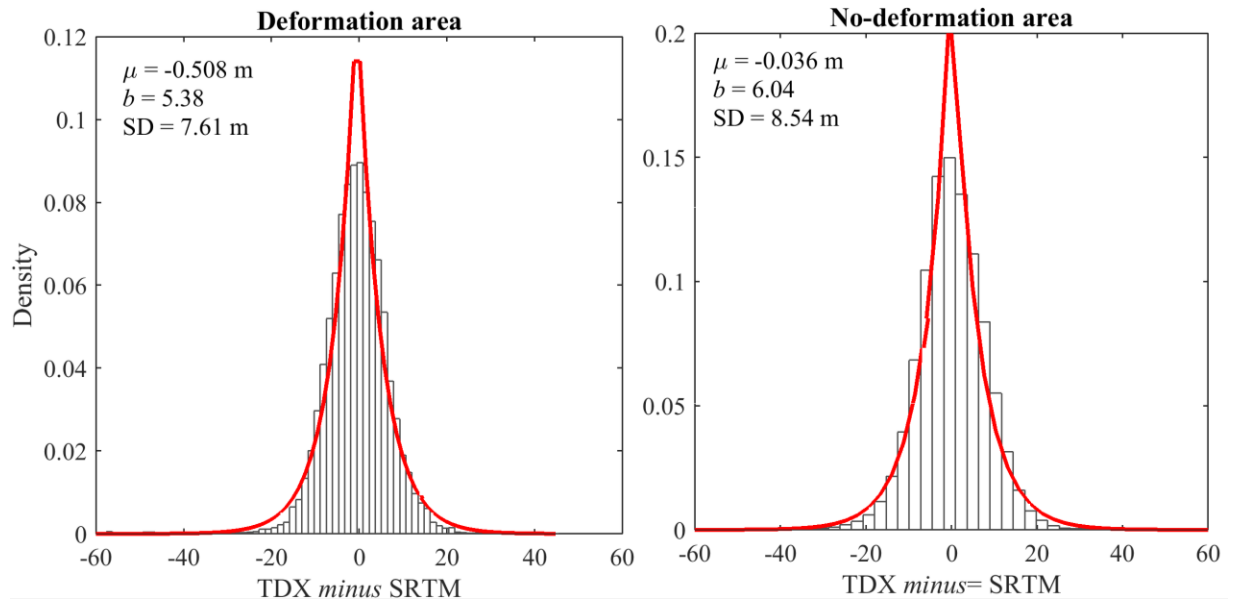
261

262

263

264

The histograms of the difference between the corrected TDX *minus* SRTM models are shown in Figure 4. We performed the one-sample Kolmogorov-Smirnov test to verify the hypothesis that the differences follow a normal distribution. The result suggests that the differences do not follow a normal distribution at the 5% significance level. Instead, we use the Laplace probability density function (pdf) to model the histogram. The Laplace pdf is controlled by μ - the location parameter and b - the scale parameter. The maximum likelihood estimator of μ is the sample median, and the estimator of b is the mean absolute deviation from the location parameter (Robert & Norton, 1984). The variance of difference is $\sigma^2 = 2b^2$.



265

266 Figure 4. Histograms of differences between TDX *minus* SRTM for the deformation and no-
 267 deformation areas. The Laplace pdf curves, including the location parameter (μ), scale parameter
 268 (b), and the standard deviation (SD, for the deformation (a) area, and no-deformation area (b) are
 269 also shown.

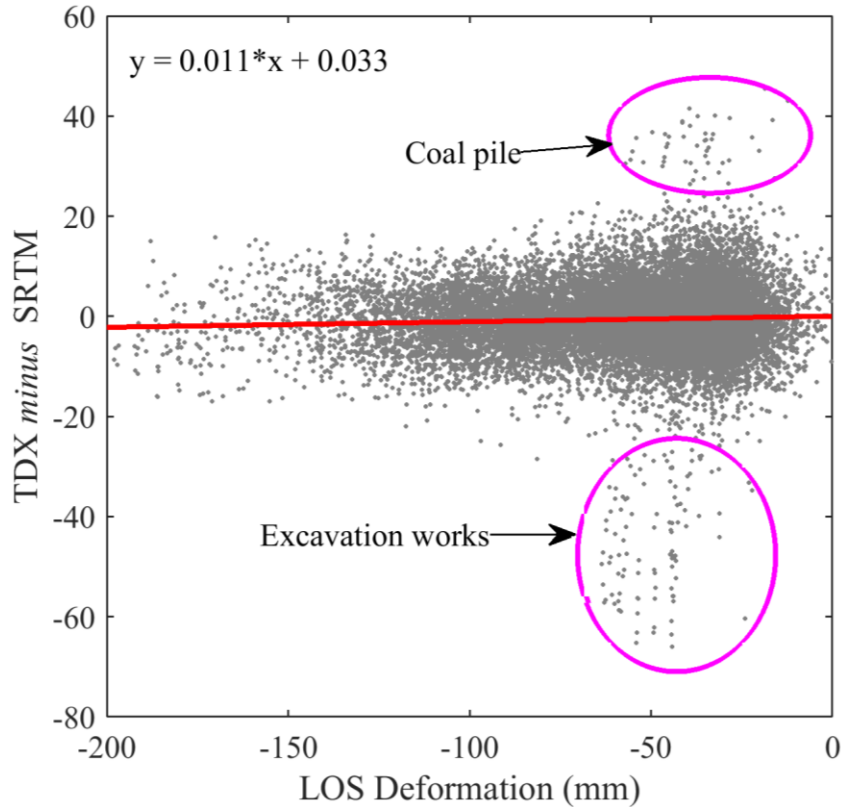
270 The calculations yielded the location parameter (approximate average difference) = -
 271 0.508 ($\sigma = 7.61$) m, and -0.036 ($\sigma = 8.54$), for the deformation and no-deformation area,
 272 respectively.

273 The average difference in the deformation area is smaller than in the no-deformation area
 274 by -0.472 m (= -0.508 + 0.036), suggesting that TDX contains the deformation signal or
 275 anomaly. To verify if this observation is statistically significant, we conducted a hypothesis test.
 276 The null hypothesis is (H_0): The average difference TDX *minus* SRTM $\mu = 0$ m. The alternative
 277 hypothesis is H_A : The average difference $\mu < 0$ m. To perform the test, we randomly selected
 278 1000 pixels in the no-deformation area. The mean difference for these random points was -0.495
 279 m ($s = 7.78$ m). We found the p -value = 0.025 < 0.05 or the confidence level of 95%. These
 280 results allows us to reject the null hypothesis at the 95% confidence level, which means that the
 281 difference TDX *minus* SRTM within deformation and no-deformation areas are statistically
 282 significant.

283 3.3 Difference vs. Deformation

284 Figure 5 shows a scattergram of the difference TDX *minus* SRTM vs. LOS deformation.
 285 A linear trend suggests a relationship between both variables. The Spearman's correlation test for
 286 the deformation area produced correlation coefficient = 0.045 with p -value = $5.2231 \times 10^{-9} < 0.01$.

287



288

289 Figure 5. TDX *minus* SRTM vs. LOS deformation, including a regression line. The correlation
 290 coefficient = 0.045, p -value = $5.2231 * 10^{-9} < 0.01$ (Spearman's test).

291 The pink ellipses in Figure 5 delineate outliers (that were considered in the hypothesis
 292 tests). A detailed inspection of the outliers determined that they are not related to the land
 293 deformation, but to the open pit excavations and piling of a byproduct of the coal power plant at
 294 Çatalağzı.

295 4 Conclusions

296 To the authors' knowledge, this is the first study to use the global digital elevation
 297 models to identify land deformations of the order of a few cm yr^{-1} . It is a straightforward
 298 approach for which the basic requirement is that there be a sufficient period between when
 299 selected DEMs were captured. In our case, the lapse is approximately ten years. As a test field,
 300 we used a region exposed to long-term underground mining-induced land deformation. Still, this
 301 approach could be applied to identify any other type of deformations, either uplift or subsidence.
 302 The causes of land deformation may include tectonic-, seismic-, landslides-, and volcanic-
 303 induced topography change over time. Since the LOS deformation occurred within a 20-month
 304 period, the average velocity = -68.6 mm over 20 months or -41.2 mm yr^{-1} . Considering this value
 305 in the context of the average difference between TDX and SRTM, which is approximately -472
 306 mm and appeared over approximately 168 months or -33.7 mm yr^{-1} , one can conclude that the
 307 results are consistent (the vertical component of the LOS deformation vector is smaller than the
 308 LOS vector).

309 The sensitivity of this method to identify land deformation depends on the accuracy of
 310 the DEMs used. A key and variable component of the accuracy of a DEM is the target-induced
 311 error (see Equation 1), which depends on the pixel size and local slope. This fact justifies the
 312 statement that for a given pair of DEMs (e.g., SRTM and TDX), the sensitivity of the method
 313 depends on the roughness of terrain: Higher slopes limit the sensitivity of the technique. The
 314 average slope in our case was 12.4° .

315 We have also tested the AW3D30 m DEM (Tadono et al., 2016) against SRTM. The
 316 obtained results (not shown here) were similar, suggesting that other DEMs can be used for
 317 similar studies of land deformations anywhere in the world.

318 To conclude, this paper has proven the effectiveness of this method to detect land
 319 deformation using readily available DEMs. By developing a dedicated software using artificial
 320 intelligence that implements this technique, it is possible to save time and costs to construct the
 321 DInSAR-based deformation raster.

322 **Acknowledgments, Samples, and Data**

323 The authors declare no and real or perceived financial conflict of interest.

324 The authors are grateful to Prof. Manfred Buchroithner for his helpful comments. Datasets
 325 for this research are available in Becek et al., (2020).

326 **References**

- 327 Amelung, F., Galloway, D. L., Bell, J. W., Zebker, H. A., & Lacznik, R. J. (1999). Sensing the
 328 ups and downs of Las Vegas: InSAR reveals structural control of land subsidence and
 329 aquifer-system deformation. *Geology*, 27(6), 483–486. [https://doi.org/10.1130/0091-7613\(1999\)027<0483:STUADO>2.3.CO;2](https://doi.org/10.1130/0091-7613(1999)027<0483:STUADO>2.3.CO;2)
- 331 Arca, D., Kutoğlu, Ş. H., & Becek, K. (2018). Landslide susceptibility mapping in an area of
 332 underground mining using the multicriteria decision analysis method. *Environmental*
 333 *Monitoring and Assessment*, 190(12). <https://doi.org/10.1007/s10661-018-7085-5>
- 334 Avsar, N. B., Jin, S., Kutoğlu, Ş. H., & Gurbuza, G. (2017). Vertical land motion along the Black
 335 Sea coast from satellite altimetry, tide gauges and GPS. *Advances in Space Research*,
 336 60(12), 2871-2881.
- 337 Bayık, C., Becek, K., Mekik, C., & Ozendi, M. (2018). On the vertical accuracy of the ALOS
 338 world 3D-30m digital elevation model. *Remote Sensing Letters*, 9(6), 607–615.
 339 <https://doi.org/10.1080/2150704X.2018.1453174>
- 340 Becek, K. (2008). Investigating error structure of shuttle radar topography mission elevation data
 341 product, *Geophysical Research Letters*. 35, L15403.
 342 <https://doi.org/10.1029/2008GL034592>
- 343 Becek, K., Koppe, W., & Kutoğlu, Ş. H. (2016). Evaluation of vertical accuracy of the
 344 WorldDEM™ using the runway method. *Remote Sensing*, 8(934).
 345 <https://doi.org/10.3390/rs8110934>
- 346 Becek, K. (2011). *Biomass representation in synthetic aperture radar data sets: a*
 347 *comprehensive study of biomass-induced elevation bias in DEMs derived using synthetic*
 348 *aperture radar interferometry*. Saarbrücken, LAP Lambert Academic Publishing.

- 349 Becek, K. (2014). Assessing global digital elevation models using the runway method: The
350 advanced spaceborne thermal emission and reflection radiometer versus the shuttle radar
351 topography mission case. *IEEE Transaction on Geoscience and Remote Sensing*, 52(8),
352 4823–4831. <https://doi.org/10.1109/TGRS.2013.2285187>
- 353 Becek, K., Kutoğlu, Ş. H., Glabicki, D., Bayık, C., Blachowski, J., & Abdikan, S. (2020).
354 Zonguldak, Turkey: Mining-induced land deformation in 2018-2019 - Sentinel 1 SBAS
355 results. Mendeley Data, v1, <https://doi.org/10.17632/szhw6k2bsv.1>
- 356 Berardino, P., Fornaro, G., Lanari, R. & Sansosti, E. (2002). A new algorithm for surface
357 deformation monitoring based on small baseline differential SAR interferograms. *IEEE*
358 *Transaction on Geoscience and Remote Sensing*, 40(11), 2375–2383.
359 <https://doi.org/10.1109/TGRS.2002.803792>
- 360 Casu, F., Manzo, M., & Lanari, R. (2005). Performance analysis of the SBAS algorithm for
361 surface deformation retrieval. Proceedings of the Fringe 2005 Workshop, 28 November–
362 2 December 2005, Frascati, Italy. Available online:
363 http://earth.esa.int/fringe2005/proceedings/papers/483_lanari.pdf
- 364 Casu, F., Manzo, M., & Lanari, R. (2006). A quantitative assessment of the SBAS algorithm
365 performance for surface deformation retrieval. *Remote Sensing of Environment*. 102(3–
366 4), 195–210. <https://doi.org/10.1016/j.rse.2006.01.023>
- 367 Chen, C. W., & Zebker, H. A. (2001). Two-dimensional phase unwrapping with the use of
368 statistical models for cost functions in nonlinear optimization. *Journal of the Optical*
369 *Society of America A*, 18(2), 338–351. <https://doi.org/10.1364/JOSAA.18.000338>
- 370 Crosetto, M., Crippa, B., Biescas, E., Monseratt, O., Aguno, M., & Fernandez, P. (2005). Land
371 deformation monitoring using SAR interferometry: state-of-the-art. *Photogrammetrie,*
372 *Fernerkundung und Geoinformation*. 6, 497–510.
- 373 Crosetto, M., & Pasquali, P. (2008). DSM generation and deformation measurement from SAR
374 data. In: Li, Z., Chen, J., Baltsavias, E. (Eds) (2008). *Advances in Photogrammetry,*
375 *Remote Sensing and Spatial Information Sciences* (pp. 157–167). 2008 ISPRS Congress
376 Book. Leiden, The Netherlands, CRC Press.
- 377 ESA (2020). Sentinel online. <https://sentinel.esa.int/web/sentinel/home>
- 378 Ferretti, A., Prati, C., & Rocca, F. (2000). Nonlinear subsidence rate estimation using permanent
379 scatterers in differential SAR interferometry. *IEEE Transaction on Geoscience and*
380 *Remote Sensing*. 38(5), 2202–2012. <https://doi.org/10.1109/36.868878>
- 381 Ferretti, A., Prati, C., & Rocca, F. (2001). Permanent scatterers in SAR interferometry. *IEEE*
382 *Transaction on Geoscience and Remote Sensing*, 39(1), 8–20.
383 <https://doi.org/10.1109/36.898661>
- 384 Goel, K. & Adam, N. (2014). A Distributed Scatterer Interferometry Approach for Precision
385 Monitoring of Known Surface Deformation Phenomena. *IEEE Transaction on*
386 *Geoscience and Remote Sensing*, 52(9), 5454–5468.
387 <https://doi.org/10.1109/TGRS.2013.2289370>
- 388 Hanssen, R. F. (2001). *Radar interferometry: Data interpretation and error analysis* (vol. 2).
389 Dordrecht, The Netherlands: Kluwer Academic, 2001.

- 390 Krieger, G., Moreira, A., Fiedler, H., Hajnsek, I., Werner, M., Younis, M., Zink, M. (2007).
391 TanDEM-X: A satellite formation for high-resolution SAR Interferometry. *IEEE*
392 *Transaction on Geoscience and Remote Sensing*, 45(11), 3317–3341.
393 <https://doi.org/10.1109/TGRS.2007.900693>
- 394 Lanari, R., Lundgren, P., Manzo, M., & Casu, F. (2004). Satellite radar interferometry time
395 series analysis of surface deformation for Los Angeles, California. *Geophysical Research*
396 *Letters*, 31, L23613. <https://doi.org/10.1029/2004GL021294>
- 397 Lanari, R., Casu, F., Manzo, M., Zeni, G., Berardino, P., Manunta, M., & Pepe, A. (2007). An
398 overview of the Small Baseline Subset Algorithm: A DInSAR technique for surface
399 deformation analysis. *Pure and Applied Geophysics*, 164, 637–661. [https://doi.org/](https://doi.org/10.1007/s00024-007-0192-9)
400 [10.1007/s00024-007-0192-9](https://doi.org/10.1007/s00024-007-0192-9)
- 401 Lee, C-W., Lu, Z., Jung, H-S., Won, J-S., & Dzurisin, D. (2006). Surface deformation of
402 Augustine Volcano, 1992–2005, from Multiple-Interferogram processing using a refined
403 Small Baseline Subset (SBAS) Interferometric Synthetic Aperture Radar (InSAR)
404 Approach. In Power, J. A., Coombs, M. L., & Freymueller, J. T., (eds). *The 2006*
405 *eruption of Augustine Volcano, Alaska. U.S. Geological Survey Professional Paper 1769.*
- 406 Normand, J. C. L. & Heggy, E. (2015). InSAR assessment of surface deformations in urban
407 coastal terrains associated with groundwater dynamics. *IEEE Transaction on Geoscience*
408 *and Remote Sensing*. 53(12), 6356–6371. <https://doi.org/10.1109/TGRS.2015.2437368>
- 409 Rabus, B., Eineder, M., Roth, A., Bamler, R. (2003). The Shuttle Radar Topography Mission—A
410 new class of digital elevation models acquired by spaceborne radar. *ISPRS Journal of*
411 *Photogrammetry and Remote Sensing*, 57(4), 241–262. [https://doi.org/10.1016/S0924-](https://doi.org/10.1016/S0924-2716(02)00124-7)
412 [2716\(02\)00124-7](https://doi.org/10.1016/S0924-2716(02)00124-7)
- 413 Robert, M., & Norton, R. M. (1984). The double exponential distribution: Using calculus to find
414 a maximum likelihood estimator. *The American Statistician. American Statistical*
415 *Association*, 38(2), 135–136
- 416 Rosen, P. A., Hensley, S., Junghin, I. R., Li, F. K., Madsen, S. N., Rodriguez, E., & Goldstein, R.
417 M. (2000). Synthetic Aperture Radar Interferometry. *Proceedings of the IEEE*, 88(3),
418 333–382. <https://doi.org/10.1109/5.838084>
- 419 Sandwell, D. R., Mellors, X., Wei, T., M., & Wessel, P. (2011). Open radar interferometry
420 software for mapping surface deformation. *Eos*, 92(28), 234–235.
421 <https://doi.org/10.1029/2011EO280002>
- 422 Schwind, M., Schneider, G., Palubinskas, T., Storch, R., Muller, R., & Richter, R. (2009).
423 Processors for ALOS optical data: Deconvolution, DEM generation, orthorectification,
424 and atmospheric correction. *IEEE Transaction on Geoscience and Remote Sensing*,
425 47(12), 4074–4082. <https://doi.org/10.1109/TGRS.2009.2015941>
- 426 Tadono, T., Nagai, H., Ishida, H., Oda, F., Naito, S., Minakawa, K., & Iwamoto, H. (2016).
427 Generation of the 30 m-mesh global digital surface model by ALOS PRISM.
428 *International Archives of Photogrammetry and Remote Sensing and Spatial Information*
429 *Sciences*, XLI(B4), 157–162. <https://doi.org/10.5194/isprs-archives-XLI-B4-157-2016>

430 Yilmaz, A., & Erdoğan, M. (2018). Designing High-Resolution Countrywide DEM for Turkey.
431 *International Journal of Engineering and Geosciences*, 3(3), 98–107.
432 <https://doi.org/10.26833/ijeg.384822>

433